TRIFFID photometry of globular cluster cores – I. Photometric techniques and variable stars in M15

R. F. Butler,[1]*† A. Shearer,[2] R. M. Redfern,[1] M. Colhoun,[1] P. O'Kane,[1] A. J. Penny,[3] P. W. Morris,[4] W. K. Griffiths[5] and M. Cullum[6]

[1]*Department of Physics, University College Galway, Galway, Ireland*
[2]*Information Technology Centre, University College Galway, Galway, Ireland*
[3]*Rutherford Appleton Laboratory, Chilton, Didcot, Oxon OX11 0QX*
[4]*Department of Physics, University of Durham, South Road, Durham DHI 3LE*
[5]*Department of Physics & Astronomy, University of Leeds, Leeds LS2 9JT*
[6]*European Southern Observatory, Garching, Karl-Schwarzschild Straße 2, D-85748 Garching bei, München, Germany*

ABSTRACT

The Galway/DIAS Image Sharpening Camera, TRIFFID, has been used to make observations in two colours of the centre of the post-core-collapse globular cluster M15. We present here our analysis of the photometry in *B* over two seasons. We have combined the complementary qualities of the *HST*'s high astrometric precision and TRIFFID's extended coverage and photometric precision, to perform crowded-field photometry in the innermost region of M15. Our technique virtually eliminates the problem of extreme crowding which has hitherto hampered studies of the variable star populations in globular cluster cores, and thereby provides an extension of the *HST*'s capability. Candidate variables detected with the *HST* have been confirmed and monitored over longer periods. We show that most of these are RR Lyrae stars, and that one is a short-period Type II Cepheid (the third to be discovered in M15). Our photometric study also produced evidence of a similar number of new variables. These also appear to be RR Lyrae stars, except for a possible eclipsing system. Further data from an upgraded version of TRIFFID have recently been obtained to help to refine the light curves of all these objects.

Key words: instrumentation: miscellaneous – techniques: photometric – Cepheids – stars: variables: other – globular clusters: general – globular clusters: individual: M15.

1 INTRODUCTION

Cores of globular clusters contain crucial information on the evolution of the clusters. They are also known to contain some of the more exotic stellar species, such as pulsars, X-ray sources and blue stragglers. However, our present tallies of some of the more conventional populations in the cores are still far from complete.

For example, the metal-poor cluster M15 ([Fe/H]= −2.15: Zinn 1985) is known to contain over 110 intrinsic variables, predominately of RR Lyrae type (Sawyer-Hogg 1973). However, because it is a post-core-collapse cluster with an extraordinarily dense centre ($r_c \leq 1.5$ arcsec: Sosin & King 1997), ground-based observations of variability have only been possible in its *outer* regions to date. In fact, in all such previous studies, no RR Lyrae variables have been confirmed within a radius of 18 arcsec from the core centre. V86, a

Cepheid of the W Vir type located some 13 arcsec from the centre, was detected only because it is brighter in the standard blue photographic passbands than any other star within 20 arcsec of the centre (see Fusi Pecci et al. 1980 and references therein). Furthermore, the formation of close binaries by tidal interaction in the cores of post-core-collapse clusters like M15 has long been expected theoretically (see Statler et al. 1987 and references therein). The majority of these should be dwarf novae, exhibiting characteristic photometric variability; but, again, the crowding problems have prevented the detection of any such systems from the ground. The only confirmed binary in the core of M15 is the low-mass X-ray binary X2127+119, identified as the optical variable AC211 (Auriere & Cordoni 1981).

Although the *Hubble Space Telescope* (*HST*) has observed M15 frequently, the science yield has been primarily concerned with the global properties of the core–cusp structure and the morphology of the colour–magnitude diagrams (CMDs) (see Sosin & King 1997 and references therein). However, Ferraro & Paresce (1993) suggested 19 candidate variables of uncertain type, based on their *HST/FOC* (Faint Object Camera) UV photometry obtained over a short time-span.

---

*Present address: Room 6225, Department of Mathematics and Statistics, The University of Edinburgh, James Clerk Maxwell Bulding, King's Buildings, Mayfield Road, Edinburgh EH9 3JZ.
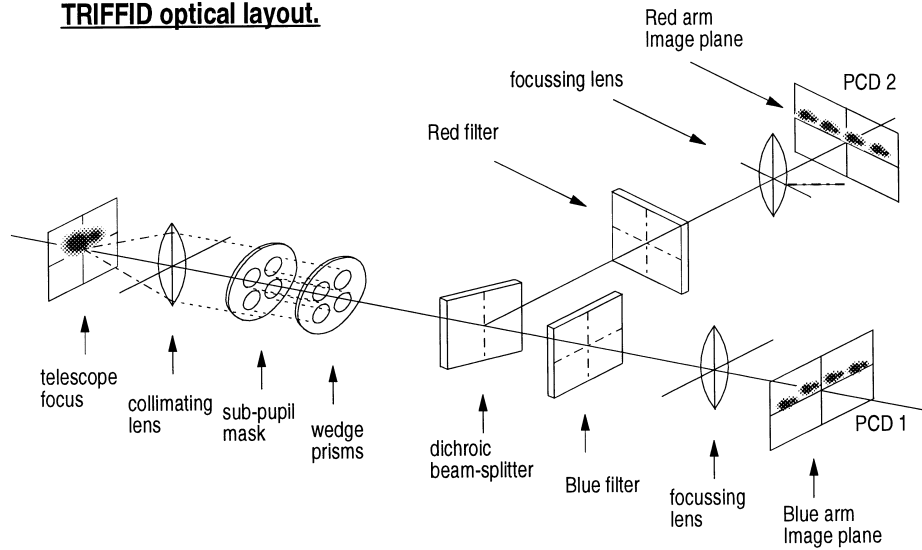†E-mail: ray@maths.ed.ac.uk

TRIFFID optical layout.

Figure 1. The TRIFFID camera.

It would therefore be of much interest both to complete the census of intrinsic variables and to search for the elusive binary variables, by conducting a systematic, sensitive photometric survey in the innermost regions. This would require both the high-resolution capabilities of the *HST* and the long-term monitoring for variability which is only really available at ground level. We are conducting such a unique study, for a number of clusters. It will be critically important that our photometry can distinguish between binaries and intrinsic variables. A study of the latter will give us important clues as to the metallicity and distance modulus of the cluster, both of which are crucial to an understanding of the age of the Galactic cluster system. A more complete survey of the RR Lyrae population would also help to resolve the nature of the relationship of the 'blue tail' population to that of the horizontal branch (HB) (Silbermann & Smith 1995). Furthermore, population comparisons between the inner and outer regions of the cluster yield vital clues to its dynamical evolution and present organization.

This paper is organized as follows. Section 2 gives a brief overview of some concepts in high-resolution imaging and the TRIFFID instrument which we have built for this purpose. Section 3 presents a summary of the observations of M15. Section 4 details the reconstruction of the images to achieve high resolution with photometric quality. Section 5 describes the new techniques employed in the photometry of the TRIFFID and archival *HST*/WFPC2 (Wide Field & Planetary Camera 2) images. Section 6 presents the results, quantifying the photometric accuracy, and illustrating the astrophysical potential of the techniques with a discussion of the variable stars detected in the cluster core.

2   POST-EXPOSURE IMAGE SHARPENING WITH THE TRIFFID INSTRUMENT

Atmospheric turbulence affects ground-based imaging by degrading the effective point spread function (PSF) of a telescope, from its diffraction limit to a PSF set by the prevailing seeing conditions. Adaptive optics (AO) systems ideally attempt to compensate fully for this wavefront distortion. However, most (80 per cent) of the degrading power is in the first-order terms, i.e. the tip and tilt of the

incoming wavefront, so significant resolution gains are possible by performing tip/tilt correction only; maximum gains are achieved when a pupil mask is used to reduce the effective aperture of the telescope, so that it matches the prevailing seeing conditions at $(3.5-4)R_0$, where R_0 is Fried's seeing parameter (Fried 1966). Tip/tilt correction can be achieved either in real time by low-order AO, or *after the exposure* by simple shift-and-add image sharpening in the manner described by Redfern (1991) and Redfern et al. (1992), a technique known as post-exposure image sharpening (PEIS). Given suitable photon-counting detectors (PCDs), PEIS is superior to low-order AO. Amongst other reasons why this is so, (i) it is possible to use complex objects or multiple stars as the 'guide star' reference, (ii) at least twice as much reference information can be obtained from any given star, and (iii) the optical path is much simpler. These factors enable much fainter reference stars to be used.

The Galway/DIAS high-resolution camera for PEIS, TRIFFID (Redfern 1991; Redfern et al. 1991, 1992), has a collimated beam containing sub-pupil masks corresponding to the prevailing $(3.5-4)R_0$ aperture, wedge prisms to redirect the sub-pupil beams, and a dichroic beam splitter to illuminate two PCDs on separate limbs: see Fig. 1. The wedge prisms allow each sub-pupil to be separately imaged on to a suitable portion of the PCDs. Within each limb, the collimated beam is brought to focus on the PCD at a suitable plate-scale. The data from the PCDs (the position and arrival time of each photon) are stored om WORM optical disks for subsequent PEIS analysis. Thus TRIFFID has a unique ability to perform time-resolved high-resolution imaging. Typically we obtain resolution improvements up to the theoretical maximum factor of 2 – or more, if there is also a significant telescope wobble component in the image motion.

3   OBSERVATIONS

Observations of the core of M15 were made in 1992 June and 1994 July using the 4.2-m William Herschel Telescope (WHT) on La Palma. TRIFFID was mounted on the GHRIL (Ground-based High-Resolution Imaging Laboratory) optical bench (Nasmyth focus). We used a MAMA (Multi-Anode Microchannel Array) detector from the European Southern Observatory (Timothy & Bybee 1985;

Table 1. Observational log: 1992 June and 1994 July. The unfiltered detector responses with the dichroic beam splitter in place are $\sim B$ for the MAMA and $\sim(V+R)$ for the RAL-PCD.

Date	Filter (MAMA, RAL-PCD)	UTC	Exposure (s)	$3.5R_0$ Aperture (m)	Image Width (arcsec)
25/6/1992	B,Hα	01:29:42	2085	1.01	0.64
	V,Hα	02:13:52	1800	1.01	0.55
	B,Hα	03:10:26	445	1.01	0.60
	None,V	04:02:32	377	1.01	0.58
	None,Hα	04:32:16	3340	1.52	0.52
27/6/1992	None,Hα	01:34:59	2634	0.92	0.58
	None,Hα	02:44:40	964	0.81	0.45
	None,Hα	03:07:26	1452	0.81	0.52
	None,Hα	03:36:00	1515	0.81	0.60
	None,Hα	04:20:00	1827	1.01	0.61
28/6/1992	None,Hα	01:31:52	525	0.81	0.54
	None,Hα	01:48:37	1881	0.81	0.54
	None,Hα	02:33:24	1837	0.81	0.38
	None,Hα	03:32:00	309	0.92	0.56
	None,Hα	03:44:47	3175	0.92	0.52
	None,Hα	04:41:11	1329	0.81	0.51
15/7/1994	None,None	22:55:22	1533	0.62	0.69
	B,R	23:22:16	1808	0.62	0.54
16/7/1994	B,R	00:05:57	1976	0.62	0.45
	B,V	01:51:02	1307	0.70	0.57
	B,R	02:18:53	268	0.70	0.52
	B,R	02:24:51	3792	0.70	0.58
	B,R	03:57:25	1483	0.70	0.62
	B,V	04:26:12	1618	0.70	0.71
	B,R	23:00:46	1801	0.62	0.75
17/7/1994	B,V	00:33:59	3140	0.62	0.58
	B,R	01:28:55	1760	0.62	0.48
	B,V	02:25:24	260	0.62	0.42
	B,V	02:30:43	1218	0.81	0.47
	B,R	02:52:55	1819	0.81	0.51
	B,V	03:25:55	331	0.81	0.49
	B,V	04:14:39	1813	0.70	0.62
	B,V	04:45:39	338	0.70	0.56
18/7/1994	B,R	00:12:30	2702	0.62	0.67
	B,V	01:44:25	1797	0.62	0.58
	B,R	03:33:04	1116	0.62	0.56
	B,V	03:53:17	3650	0.62	0.59
	B,R	04:56:21	1686	0.62	0.56

Cullum & Wampler 1990) on the blue limb and a CID (Charge Injection Device)-based photon-counting system from the Rutherford Appleton Laboratories (Read et al. 1995; Carter et al. 1990) on the red limb. On all nights the seeing was good and occasionally superb; conditions were always photometric. Table 1 shows a log of the observations. The image widths (FWHM) quoted are those obtained after PEIS, and typically represent a factor of 2 improvement over the unsharpened data – sufficient to perform photometry right into the core of M15 with the particular technique described in Section 5.2. In order to maximize the light throughput – essential for the sharpening process as well for the photometry – the GHRIL image derotator was removed. As the position and arrival time of each photon were recorded it was possible to derotate the images after the observations were made. In 1992 TRIFFID was operated with four sub-pupils and a field of view of 14 arcsec. In 1994 only one sub-pupil was used with a field of view of 19×70 arcsec². Flat-fields were recorded during twilight on the sky and on the inside of the dome.

4 RECONSTRUCTING THE TRIFFID IMAGES

The images were reduced with our in-house PEIS software

(Redfern et al. 1989; Morris 1995) to produce a series of CCD-like images with improved resolution. The first step was initially to derotate and integrate 120 s of data. From the resultant image, typically 5 to 10 reference stars were selected whose motions would be tracked in the next step – the shift-and-add sharpening. In this step the software builds a composite reference star consisting of the reference stars' photons from the current millisecond 'frame' plus their photon contributions, weighted using a Wiener filter, from the previous and subsequent 256 ms. The resulting composite reference star image is then convolved with a Lorentzian function and finally the reference star's current position is calculated by fitting a Gaussian function. The sharpened image is therefore built up by integrating the data for each millisecond, once they have been derotated and shifted to cancel the reference star movement. The same sharpening shifts are scaled and rotated appropriately to integrate the image from the second detector.

Flat-fielding was performed during the same step as the sharpening. The arrival position of each photon was referenced to the inverse-normalized detector flat-field, and the photon was assigned the intensity at that flat-field position before derotation, shifting and
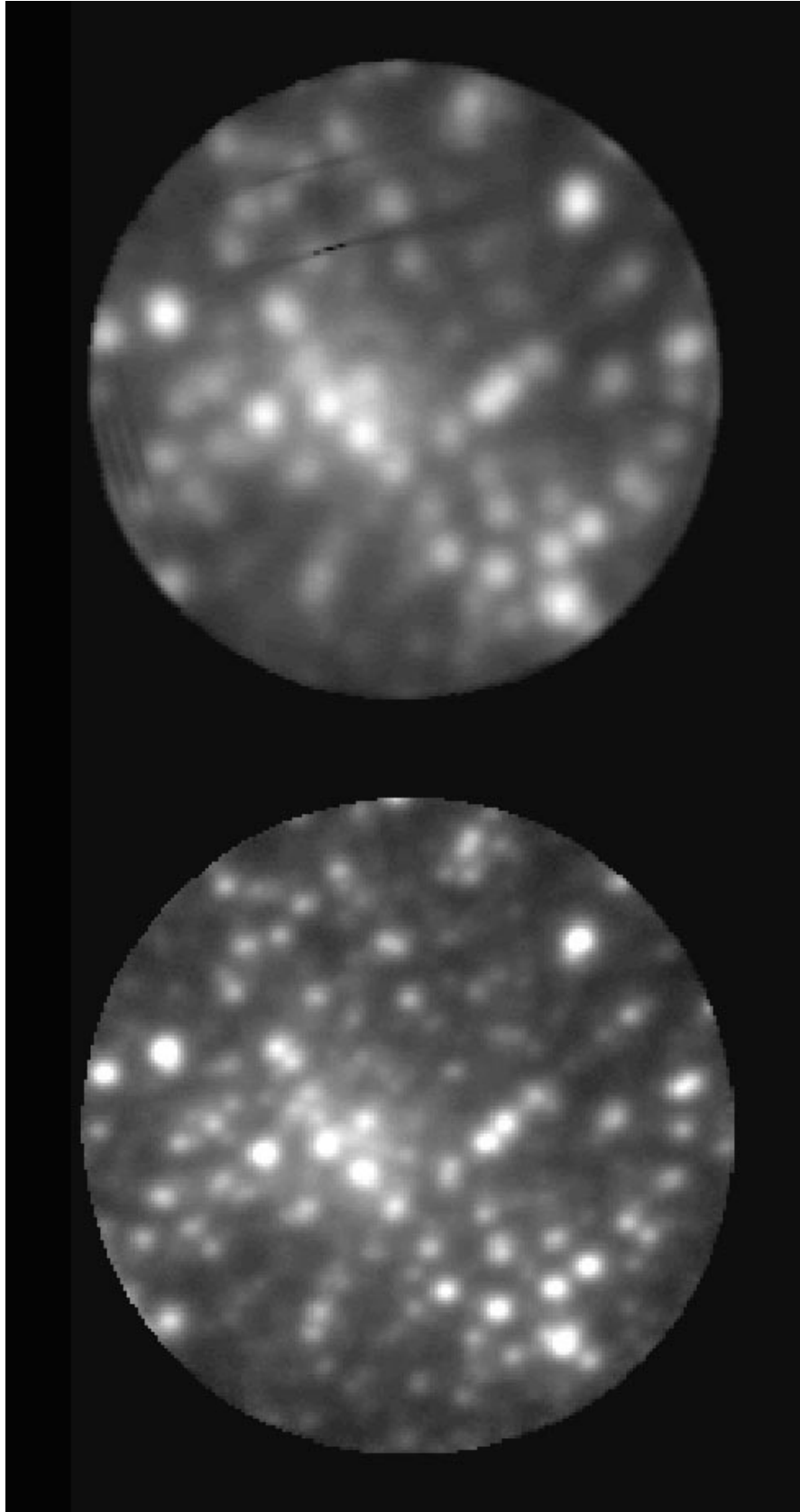
Figure 2. 1992 June data: one image, unsharpened (top) and sharpened (bottom). North is up and east is to the left.
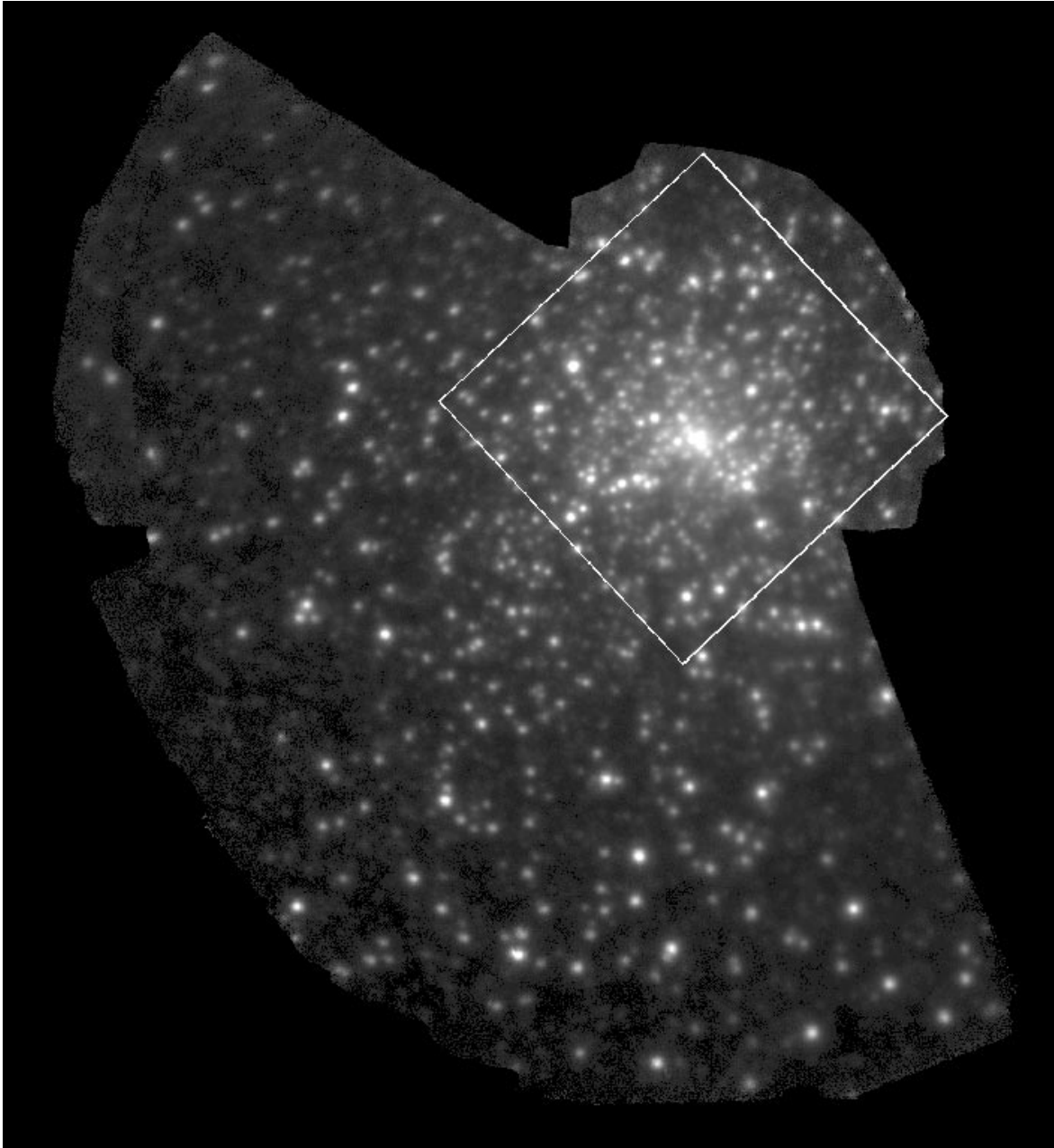
Figure 3. 1994 July data: composite of all sharpened images, with PC1 field boundary shown. North is up and east is to the left.

integration into the output image. 'Hot' pixels on the flat-field were zeroed beforehand.

Finally, the sharpened, flat-fielded images were corrected for unequal exposure at the image edges (resulting from altazimuthal field rotation and sharpening shifts) by dividing exposure masks into them. These masks are computed from the pre-calculated sharpening shifts stored in a quality file. They also correct for the light lost by the few 'dead' and 'hot' (zeroed) pixels. This step produces images which are photometric throughout (with the sole penalty of increased Poissonian noise towards their edges).

The total computation time for all these steps on a Hewlett Packard Apollo 735 is of the order of 10 times the exposure time of the image and is dominated by the sophisticated calculation of the shifts. The alternative simple centroiding algorithm can sharpen the

data in pseudo-real time, but it is slightly less effective at improving the image resolution.

To avoid phase smearing in the photometry of shorter period variables, the longer exposures of ≥ 2400 s were split so that two equal-duration images were produced (again using the quality file).

In the case of the 1992 June data, the three sharpest sub-pupil images from each exposure were co-added after being reconstructed as described above. Thus, for this mode of operating TRIFFID, signal-to-noise ratio was gained at the expense of field of view.

Fig. 2 shows images made by co-adding three of the four sub-pupil images from the best 1992 June exposure. At the top is the unsharpened, derotated image, showing the 'raw' prevailing seeing (0.70 arcsec). At the bottom is the sharpened, derotated image, showing the resolution improvement to 0.38 arcsec. We can also see

the effect of the exposure mask, which has corrected this sharpened image for both the detector defects and the vignetted edge seen in the top image.

Fig. 3 shows a composite sharpened image made from all of the 1994 July data; the average stellar resolution is ~0.5 arcsec. The corresponding *HST*/WFPC2 (PC1 chip) field of view is also shown as a superimposed white frame. All of the subsequent photometry discussed in this paper is of the stars *within this frame only*.

5 STELLAR PHOTOMETRY IN THE CORE OF M15

5.1 *HST*/WFPC2 archival images

The crowded-field photometry package DAOPHOTII (Stetson 1994), as implemented in the external IRAF package DIGIPHOTX, was used for all the photometric reductions.

Photometry was first performed on archival *HST*/WFPC2 images of M15 in two filters – F439W which approximates to *B*, and F555W which approximates to *V*. These data were obtained under *HST* proposal GO 5324 (PI Brian Yanny). The first 43 rows and 51 columns of these images were cropped to remove the noise area at the edges due to the WFPC2 pyramid. Our investigations of photometric techniques on M15 WFPC2 data have led to the same basic conclusion as that in Guhathakurta et al. (1996) (on this same WFPC2 data set) who describe an 'optimal hybrid method' combining profile and aperture photometry. However, we have modified this approach to achieve better results on the fainter stars. Our novel star detection technique uses maximum entropy (MEM) deconvolution on an expanded grid using either empirical PSFs or synthetic PSFs computed using the TINY TIM software package (Krist & Hook 1996) – depending on the degree of spacecraft pointing jitter and optical tube assembly 'breathing', as well as the crowding which limits the cleanliness of initial empirical PSF estimates. A more complete description of these techniques can be found in Butler & Shearer (in preparation). In the case of M15, synthetic PSFs produced fewer artefacts around bright stars. This allowed us to detect significantly more faint stars even in the most crowded regions. The validity of these detections is confirmed by the tightness and population of the main sequence on the final CMD.

These steps provided a complete astrometric and photometric reference for 10 722 stars on the PC1 chip, over the central 34×34 arcsec^2 field of M15.

5.2 TRIFFID images

The central density of M15 is one of the highest of known globular clusters (Guhathakurta et al. 1996), which combined with its distance of 11.5 kpc presents a severe challenge to ground-based photometric studies.

Apart from the marked resolution improvement, a number of other benefits to crowded-field photometry accrue from the use of TRIFFID. Because the technique uses PCDs with a high-throughput data collection system, we do not suffer from the saturation and charge-bleeding problems which have limited previous CCD or photographic studies of globular cluster cores. On telescopes of ≥ 2.5-m aperture the requirement of stopping down to ≤ 1-m aperture permits us to image without diffraction from the secondary and its supporting spider. For the same reason, we can preferentially utilize those sections of the primary mirror with the best optical figure. The oversampled pixel scale (0.075 arcsec pixel^{-1}) yields smooth stellar profiles, even in excellent seeing. For these three

reasons, the resulting PSFs are compact in overall extent, smooth, and easy to model accurately.

The procedure followed for *each* image was as follows. An initial PSF was obtained using standard recursive techniques. The star list at this point consisted only of those stars that had been located by DAOFIND – typically around 200 on the 14 arcsec field images, and around 550 on the sections of the wider field images which overlapped the *HST*/PC1 field. Then the image and its PSF were fed into the MEM (maximum entropy – Wu 1994) or LUCY (Lucy–Richardson – Lucy 1974, 1992) restoration tasks in STSDAS. Although not photometrically reliable, the restored image provided accurate stellar astrometry because of its improved sharpness. This enabled us to determine a high-order coordinate transformation (accounting for relative geometrical distortion) between the image and the *HST*/WFPC2 field, by mapping bright stars common to both. 50–80 common stars were selected from each of the restored 1992 June images and 130–240 stars from each of the 1994 July images. The application of this transformation to the *HST*/PC1 star list, using GEOXYTRAN in the external IRAF pachage IMMATCH (Phillips & Davis 1995), now provided a positionally accurate star list for the TRIFFID image, virtually complete to magnitude $B \approx 21$ and with good initial magnitude and sky background estimates and unique ID numbers for each star. Next, the background estimates were scaled up appropriately, the PSF was redetermined using the new star IDs, and the transformed list was fitted by DAOPHOTII/ ALLSTAR as a *single* group. Normally ALLSTAR is allowed to subdivide the star list into smaller groups of ~ 100–200 stars, to avoid prohibitive computer memory requirements; however, if the crowding is extreme this results in errors at the boundaries of each group, so we enhanced ALLSTAR to enable it to cope with groups of 3000+ stars, when recentring and merging are not required. These enhancements are incorporated into the next IRAF/DIGIPHOTX release. This technique enabled the attempted fitting of up to 10 times *more* stars in the core region than one could originally detect on the TRIFFID image, greatly improving the photometric scatter.

Zero-pointing of the instrumental magnitudes from each image was performed by calibrating the sequence of stars in the range $m_{F439W} = 16$–18 against their counterparts in the *HST* list: a magnitude offset was applied to standardize each set of instrumental magnitudes to the *HST* flight system. Large-amplitude variable stars were identified and excluded from the determination of the magnitude offset by using a histogram of the individual offsets, and the median offset was then calculated within a range that appeared to represent a normal distribution of magnitude scatter for non-variable stars. In this way, a large sample of star measurements per TRIFFID image were used to give robust statistics for the calibration.

6 RESULTS

6.1 Post-processing of the photometry

The proportion of on-image stars in the master list that were successfully measured varied between images, but was largely complete to $m_{F439W} \sim 19$ even in the core – e.g. for our sharpest image the proportion was 93 per cent, within 4 arcsec of the centre. As the list contained stars fainter than our observing limit – a limit set by crowding, and in some cases exposure depth – ALLSTAR rejected stars whose brightness was estimated to be more uncertain than $\leq 2.0\sigma$ above zero.

Some precautions needed to be taken before the photometry was used to determine average magnitudes, search for variability, etc.
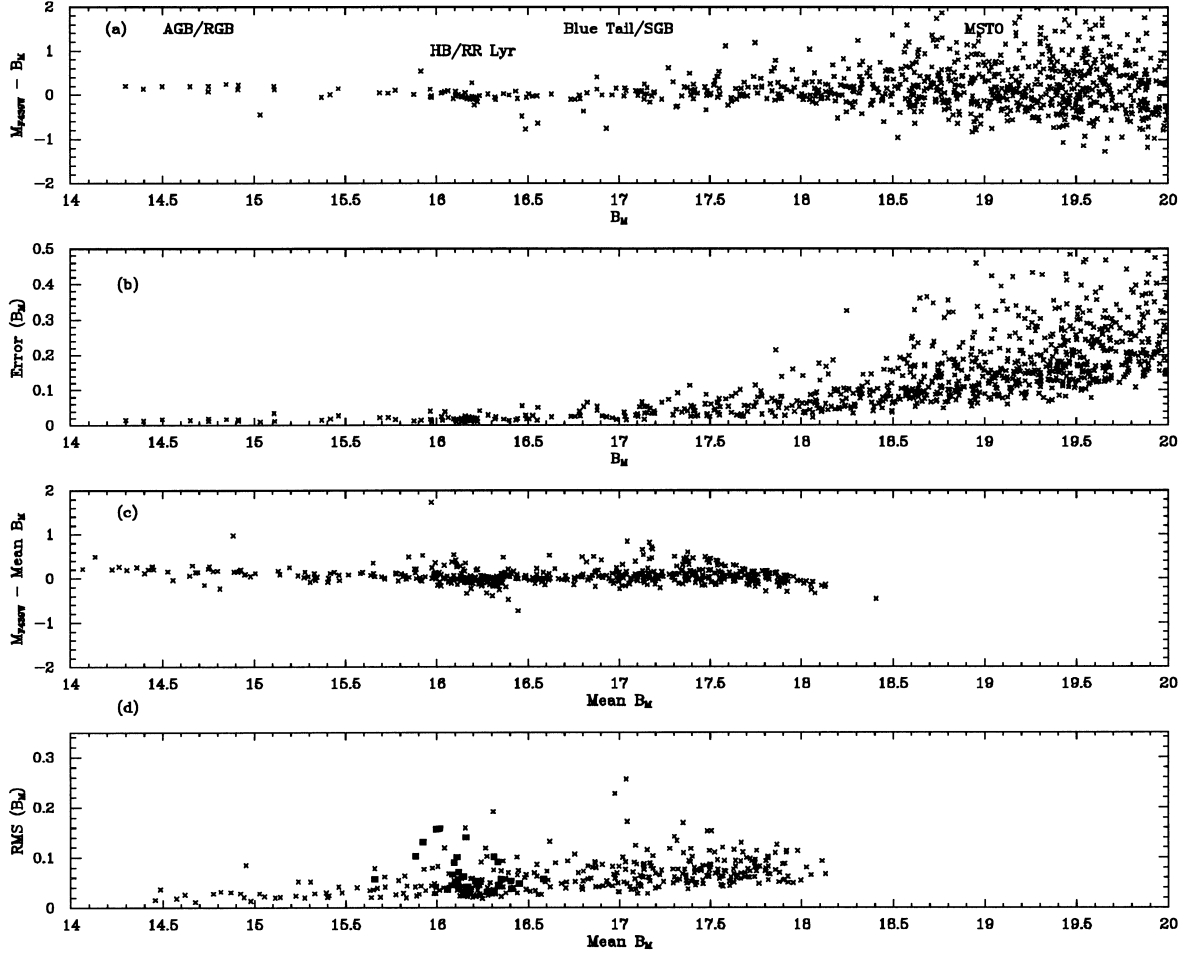
Figure 4. Assessment of TRIFFID/MAMA photometry, as described in Section 6.

Table 2. Magnitude and period characteristics of the *HST* candidate variable stars. The ID_{HST} column lists the Ferraro & Paresce (1993) IDs.
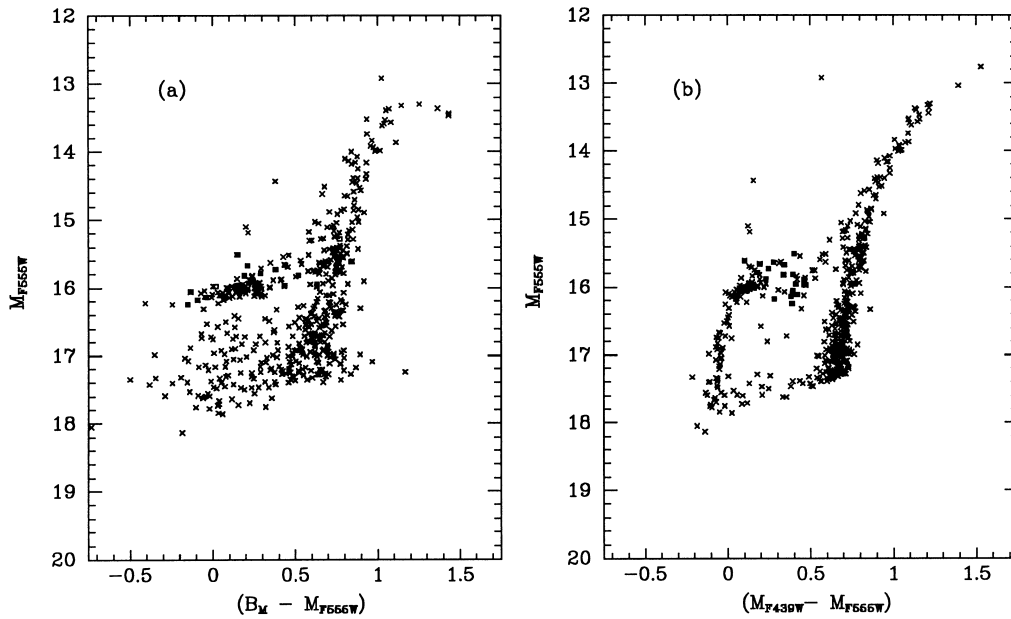
ID	ID_{HST}	X_{PC1} (pixel)	Y_{PC1} (pixel)	Radius (arcsec)	m_{F439W} (mag)	B_M (mag)	rms (B_M) (mag)	Epoch (MJD)	Period (day)	Amplitude (mag)	Type
5719	$V1_{HST}$	397.085	346.567	1.43	16.37	16.11±0.05	0.05	48799.16	0.233	0.79	RRc
4144	$V2_{HST}$	731.927	264.533	14.29	16.45	15.92±0.05	0.13	49550.2	0.297	1.05	RRc?
5039	$V3_{HST}$	675.789	312.137	11.35	16.21	16.33±0.06	0.09	49551.21	0.213	0.73	RRc?
7648	$V4_{HST}$	547.022	448.939	7.15	16.63	16.09±0.04	0.09	48800.12	0.579	1.37	RRab
8305	$V5_{HST}$	518.804	487.624	7.65	16.12	16.12±0.05	0.07	48799.14	0.263	0.92	RRc?
8284	$V6_{HST}$	474.390	487.503	6.78	16.47	16.35±0.03	0.06	49549.09	0.404	0.80	RRc
6443	$V7_{HST}$	529.360	384.913	4.92	16.46	16.08±0.04	0.07	49550.07	0.602	0.91	RRab
5380	$V8_{HST}$	557.057	330.296	5.89	15.98	16.11±0.04	0.04	49549.02	0.373	0.86	RRc
8126	$V9_{HST}$	371.438	477.417	6.53	16.44	16.41±0.04	0.04	48798.07	0.698	1.08	RRab
7224	$V10_{HST}$	372.944	427.116	4.48	15.71	16.45±0.04	0.05	48800.2	0.336	0.90	RRc
4031	$V11_{HST}$	419.171	258.507	4.00	16.53	16.40±0.04	0.05	49548.98	0.705	1.06	RRab
8297	$V13_{HST}$	248.663	487.669	10.42	15.85	16.10±0.04	0.05	49551.21	0.321	0.78	RRc
4910	$V14_{HST}$	340.564	305.671	4.40	15.92	16.31±0.08	0.10	48799.14	0.830	1.46	RRab?
3663	$V15_{HST}$	246.717	240.641	9.56	16.52	16.10±0.05	0.05	49551.08	0.367	0.89	RRc
4477	$V16_{HST}$	371.163	282.973	3.87	15.91	15.66±0.03	0.06	49548.98	1.280	1.38	AHB

First, we rejected all measurements of stars within 10 pixels of the curved image boundaries, as they were likely to be skewed by unfitted stars whose centres lay just off-image. Secondly, we rejected measurements of the sharpening reference stars and all much fainter stars within a 15-pixel radius of them, because their oversharpened cores had drawn flux from their wings. While this was undoubtedly unwarranted in cases of excellent seeing (large R_0 and hence high count rates for sharpening), we maintained this severe exclusion rule to ensure that spurious variable detections would not occur later. We never used the bright stars within the

Table 3. Magnitude and period characteristics of the other variable stars, primarily new discoveries.

ID	Previous ID (old variables)	X_{PC1} (pixel)	Y_{PC1} (pixel)	Radius (arcsec)	m_{F439W} (mag)	B_M (mag)	rms (B_M) (mag)	Epoch (MJD)	Period (day)	Amplitude (mag)	Type
135	-	621.686	8.712	17.68	16.72	16.58±0.05	0.06	49549.11	0.163	0.59	Ecl?
565	V83?	256.275	40.643	15.95	16.43	16.11±0.04	0.10	49550.03	0.292	1.25	RRc
1417	V85	39.337	106.236	20.80	16.51	16.16±0.04	0.14	49549.97	0.618	1.10	RRab
1856	-	206.657	133.711	13.97	16.12	15.99±0.05	0.16	49551.08	0.199	0.84	RRc?
2283	-	166.399	159.925	14.62	16.01	15.88±0.05	0.10	49548.96	0.647	1.03	RRab
2411	-	241.679	167.298	11.76	16.11	16.06±0.05	0.04	49551.17	0.301	0.71	RGB
2954	-	326.150	200.408	8.09	16.34	16.32±0.05	0.03	49550.19	0.189	0.58	RGB
7229	-	472.435	426.675	4.19	16.11	16.17±0.04	0.04	49550.11	0.637	0.61	RRab?
7516	-	270.441	441.671	8.41	16.34	16.34±0.04	0.05	49550.19	0.899	1.07	RGB
7600	-	147.165	447.440	13.61	16.17	16.27±0.03	0.03	49548.98	0.272	0.33	RRc
7964	-	532.439	468.124	7.30	16.17	16.21±0.03	0.05	49550.11	0.214	0.37	RRc?
8807	-	235.403	517.622	11.76	16.36	16.14±0.03	0.06	49551.2	0.734	0.69	RRab
9245	-	392.863	544.679	9.19	16.12	16.23±0.03	0.05	49550.19	0.634	0.68	RRab
10039	-	290.235	596.073	13.01	15.97	16.08±0.03	0.04	49550.19	0.188	0.52	RRc?
10837	-	458.650	654.884	14.13	16.16	16.01±0.04	0.16	49551.08	0.224	1.27	RRc

Figure 5. CMD of M15. (a) TRIFFID: F555W, B–F555W. (b) *HST*/PC1: F555W, F439W–F555W.

core cusp itself for sharpening, to ensure that the photometry was preserved in this region.

6.2 Accuracy of the photometry

In Fig. 4, we illustrate the quality of the photometry obtained with our technique. Fig. 4(a) shows the scatter in the photometry of one TRIFFID/MAMA image against the same stars measured on the *HST*/PC1 F439W image. Despite the severe crowding – the detected stellar density ranges from *12 to 20 stars per square arcsecond* in this 14 arcsec diameter region across the cluster core – the linearity and low scatter are remarkable. Some of the scatter is in fact due to the difference between the spectral responses of the unfiltered MAMA detector and the WFPC2–F439W combination, which becomes apparent when imaging stellar populations with a broad temperature range. A number of bright variables stand out immediately – including AC211, a component of the triple system

AC214, and at least two variables at the level of the HB. Fig. 4(b) shows the magnitude errors computed for each star by DAOPHOTII/ ALLSTAR. However, by inspecting the scatter in the CMDs, we have found that one should multiply these values by about 1.5–2 for a more realistic evaluation of the photometry in very crowded regions. This is because ALLSTAR tends to overestimate the magnitudes of crowded stars near the signal-to-noise ratio limit, by underestimating the background beneath them (Shearer et al. 1996), despite the most careful PSF construction. Even so, the errors are still low enough at least to perform useful variability searches or monitoring. Fig. 4(c) shows the photometric quality for weighted-average measurements using the entire M15 data set from TRIFFID. Finally, Fig. 4(d) plots the rms magnitude deviation of each star against its mean magnitude. Because of the widely varying number of measurements per star, which results in different values of σ for the same range of magnitude fluctuation, Fig. 4(d) should only be used as a guide for indicating which
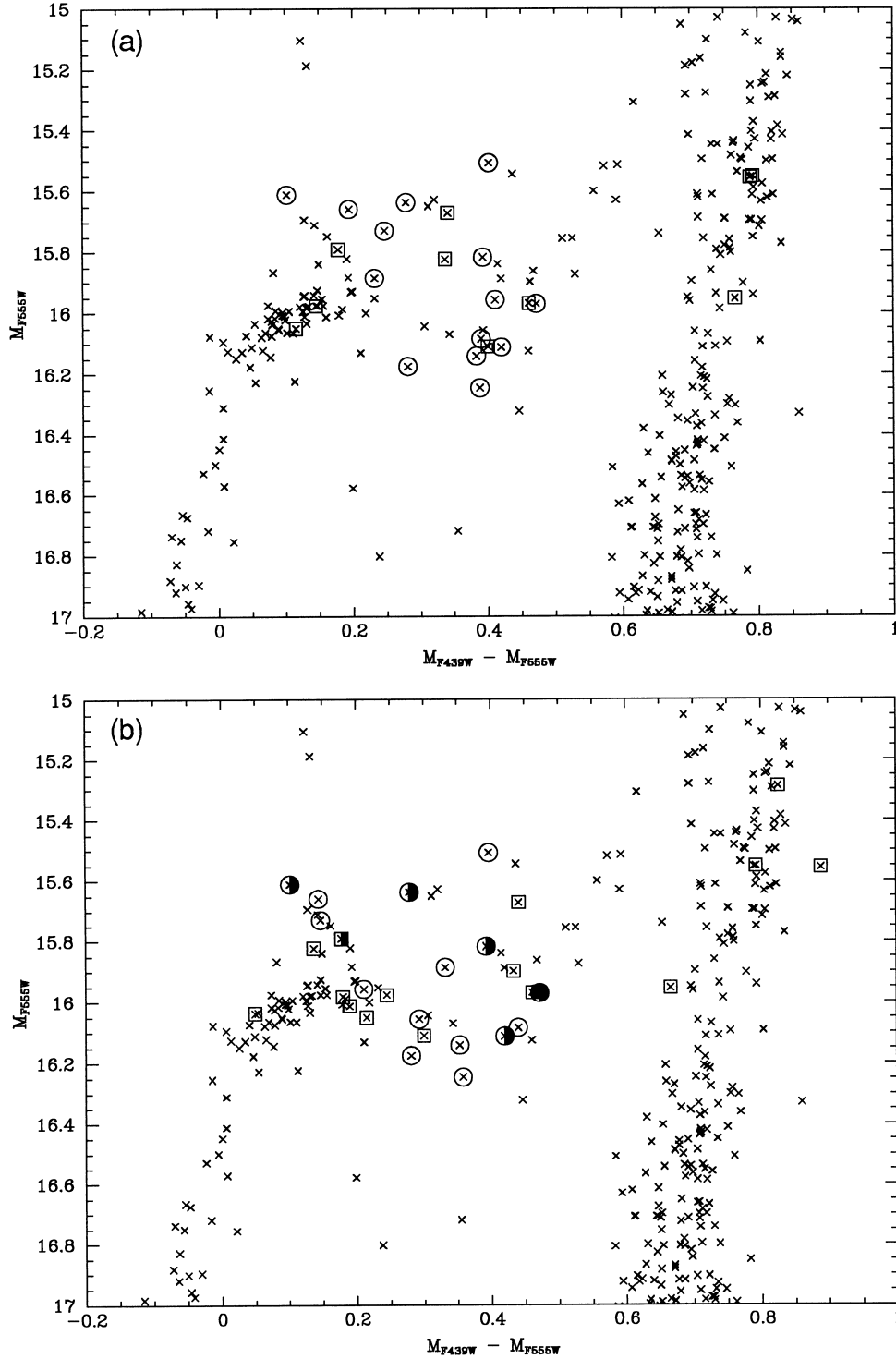
Figure 6. Location of variables on the *HST* CMD. (a) Original CMD. (b) After correction of most variables for phase (colour) lag. The circles mark the *HST* candidate variables and the squares our other variables. The variables that we could not colour-correct are plotted with half-filled symbols.

stars *might* be variables. The large deviations around the knot of stars at $B_M \sim 16$ are due mainly to the RR Lyrae population. This is also reflected in Fig. 4(c) by the increase in scatter around $B_M \sim 16$–16.5. Those stars that we believe to be variable are marked with filled squares; how we came to this conclusion is decribed next.

6.3 Search for variable stars

We examined the collated measurements of all stars brighter than $m_{F439W} \sim 18$ (including the blue tail to the HB and blue stragglers) for evidence of variability, using the PDM (phase dispersion minimization, PDM) task in IRAF. The period, amplitude and epoch were

Figure 7. Representation of PC1-F439W image of M15. The circle sizes indicate the brightness of the principal stars (binned by magnitude from $m_{F439W} = 13.5$ to 17.5). *HST* candidate variables are marked with half-filled circles; the others (primarily new discoveries) are marked with completely filled circles. The distribution of new variables correlates with our most frequently observed portions of the field, indicating that other variables might yet be discovered if more data were obtained; and, as one would expect, few of the new candidates lie in the *HST*-FOC field previously studied by Ferraro & Paresce (1993).

computed for the minimum dispersion found within an oversized period window of 0.1 to 10 d, with 0.001-d resolution. The phase curves were produced by phase-folding the data with the computed period at the computed epoch – the time at which phase 0 first occurred in the data set. To prevent excessive scatter in the light curves, some of the data points for stars closer to the core centre were excluded from the PDM analysis, on the basis of their larger error estimates (due to poorer seeing and/or short exposures). To avoid introducing any subjective bias in rejecting these poorer data, such points were systematically excluded according to the rule

$$\frac{\text{magerr}}{\sqrt{\text{radius} + 2}} < 0.03 \tag{1}$$

where 'magerr' is the error estimated by ALLSTAR, and 'radius' is the distance (in arcseconds) of the star from the core centre. The minimum number of data points upon which PDM could operate was found to be six, which unfortunately precluded several of the stars with anomalously large rms values. These had few measurements because of the variable coverage of the PC1 field – no single TRIFFID image could cover this whole 34×34 arcsec^2 region. However, as the WHT derotator had not been used, during each of the three nights in 1994 July our imagery swept out a large total field (see the composite image of Fig. 3), and therefore stars near the outer parts of the PC1 field were imaged at least once. Stars within 7-arcsec radius of the centre were observed most frequently.

The phase curve details are listed in Tables 2 and 3 for the confirmed and probable variables. The radial positions were determined by letting our star No. 5701 represent the core centre at

428.153, 345.546 in cropped PC1-image co-ordinates, since the sky background values in the PC1 photometry rose to a peak with the best radial symmetry around this particular star. We adopted the approximate PC1 pixel scale of 0.0455 arcsec pixel^{-1} (Freudling, private communication). The X and Y positions quoted are also in cropped PC1-image coordinates. It should be noted that the amplitude and epoch values are actual data points, and therefore may be inaccurate in the more sparse stellar data sets. A further caveat is that any incompletely sampled light curves – particularly the near-horizontal portions when an RR Lyrae variable is in its faint state – will tend to yield underestimated periods using PDM.

There remains the question of the other stars with large magnitude deviations, which had sufficient points to be processed by PDM but which we do not believe to be variable. The location of these in Fig. 4(d) could be explained in all cases: they had relatively few measurements, one or two of which were from the poorer images, thus biasing the σ calculation.

6.4   The colour–magnitude diagrams as an indicator of variability

Another indicator of variability is the scatter around the HB in the CMDs. The TRIFFID $B-m_{F555W}$ CMD is shown in Fig. 5(a); the *HST*/PC1 $m_{F439W}-m_{F555W}$ CMD of the same stars is shown in Fig. 5(b). In both cases only stars brighter than $m_{F439W}=18$ are plotted. The TRIFFID CMD compares very favourably with both pre-refurbishment *HST* results from M15 and an earlier attempt to combine *HST* observations with ground based ones – see figs 12 and
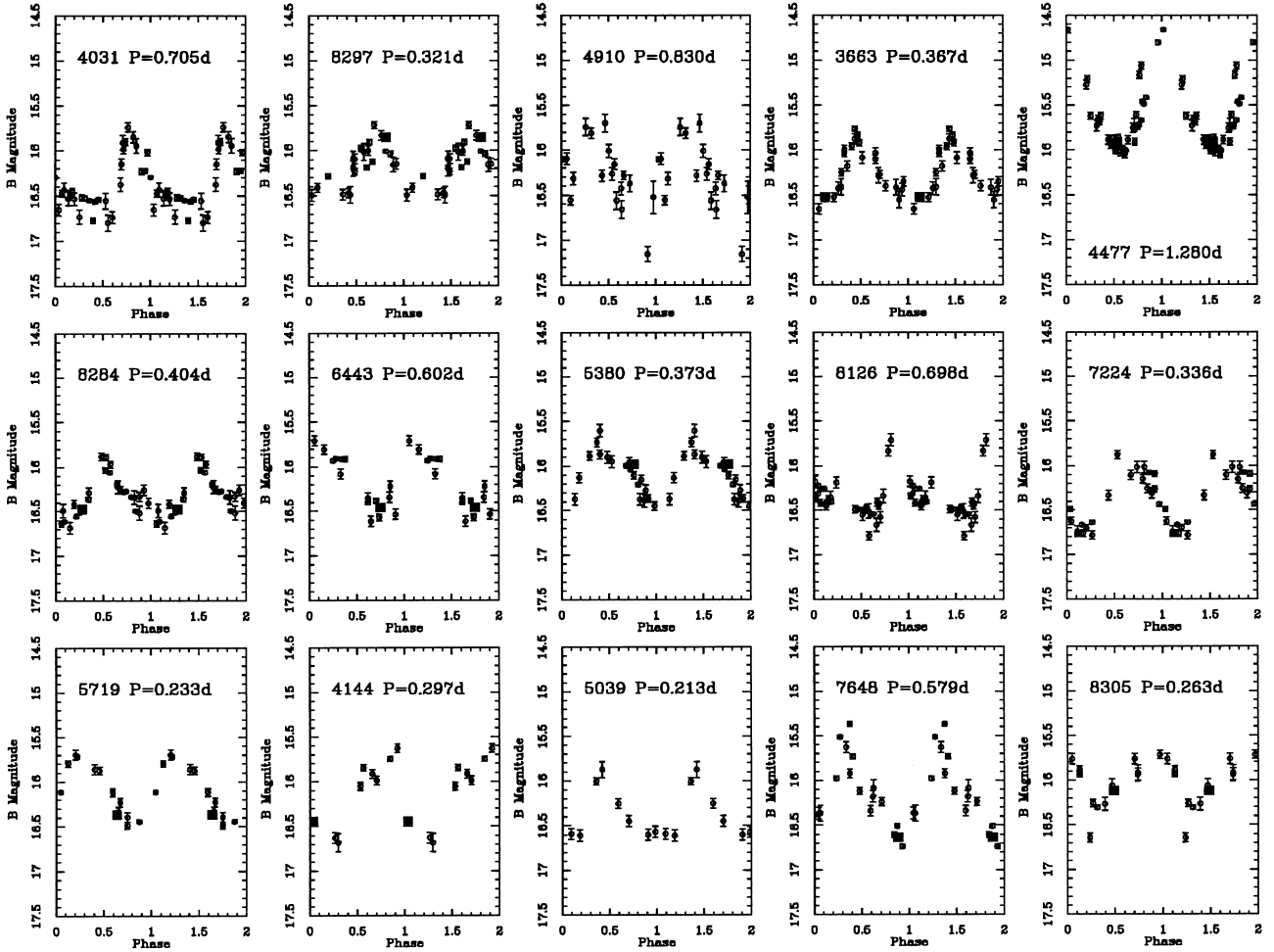
Figure 8. Intrinsic variable star light curves observed in the central region of M15: *HST* candidate variables. The corresponding m_{F439W} point is shown as a filled black square except for the stars where it did not fall in phase. The error bars plotted were computed by ALLSTAR on the basis of crowding and Poissonian noise.

13 of Yanny et al. (1994) and figs 12(b) and 21(a) of Stetson 1994. Those studies had the advantages of broader colour baselines and either additional, less-crowded stars at larger radii from the core or a selection criterion on the magnitude consistency. The tendency of DAOPHOTII to overestimate the magnitudes of stars near the signal-to-noise ratio limit (see Section 6.2) causes the gradual bias towards the blue for stars fainter than $m_{F555W} \geq 17$. However, the scatter of several bright stars bluewards of the HB is mainly due to genuine variability, as we explain next.

The single epoch of the *HST* imagery captures variables at random phases in their cycles and this contributes to scatter on the ordinate of the CMDs. Furthermore, because the F439W images were taken several minutes after the F555W images, some short-period/large-amplitude variables are likely to exhibit anomalous colours. Both of these effects can be seen in the *HST* CMD shown in enlarged form in Fig. 6(a). They make it difficult to determine whether certain of our variables are really located on the red giant branch, or whether the lag between the F555W and F439W imagery places normal RR Lyraes there by chance. To investigate these factors, we added the m_{F439W} measurements into the light curves to determine their phases, estimated the magnitudes in m_{F439W} at the earlier (m_{F555W}) epoch, and corrected the CMD. In Fig. 6(b) a much tighter sequence can now be seen, where we would expect to find RR Lyraes if the F439W and F555W images had been taken simultaneously. Certain variable

candidates could not be corrected in this way, because their m_{F439W} measurements did not fall in phase with the MAMA light curve (presumably because of the Blazhko effect or an underestimation of the period). These stars are marked with half-filled symbols.

The same factors cause some scatter around the upper red giant branch/asymptotic giant branch in the TRIFFID CMD. This is to be expected as some of these evolved stars are undoubtedly long-period variables.

Fig. 7 shows the locations of the population of variables studied in the core of M15, and Figs 8 and 9 show their light curves.

7 CONCLUSIONS

We have demonstrated a technique which can provide ground-based photometry in extremely crowded star regions. Our photometric accuracy in this difficult regime approaches that of the *HST*, but uniquely we are able to take images over a prolonged period.

In this study we have confirmed that 15 out of the 19 candidates in the Ferraro & Paresce (1993) *HST* study are regular variables, probably all of RR Lyrae type, with the exception of V16$_{HST}$ (No. 4477) whose longer period light curve (1.3 d) and brighter mean magnitude are consistent with a short-period Type II Cepheid variable – the third to be discovered in M15 (the others are V1 and V72: Sawyer-Hogg 1973). In the subclass nomenclature
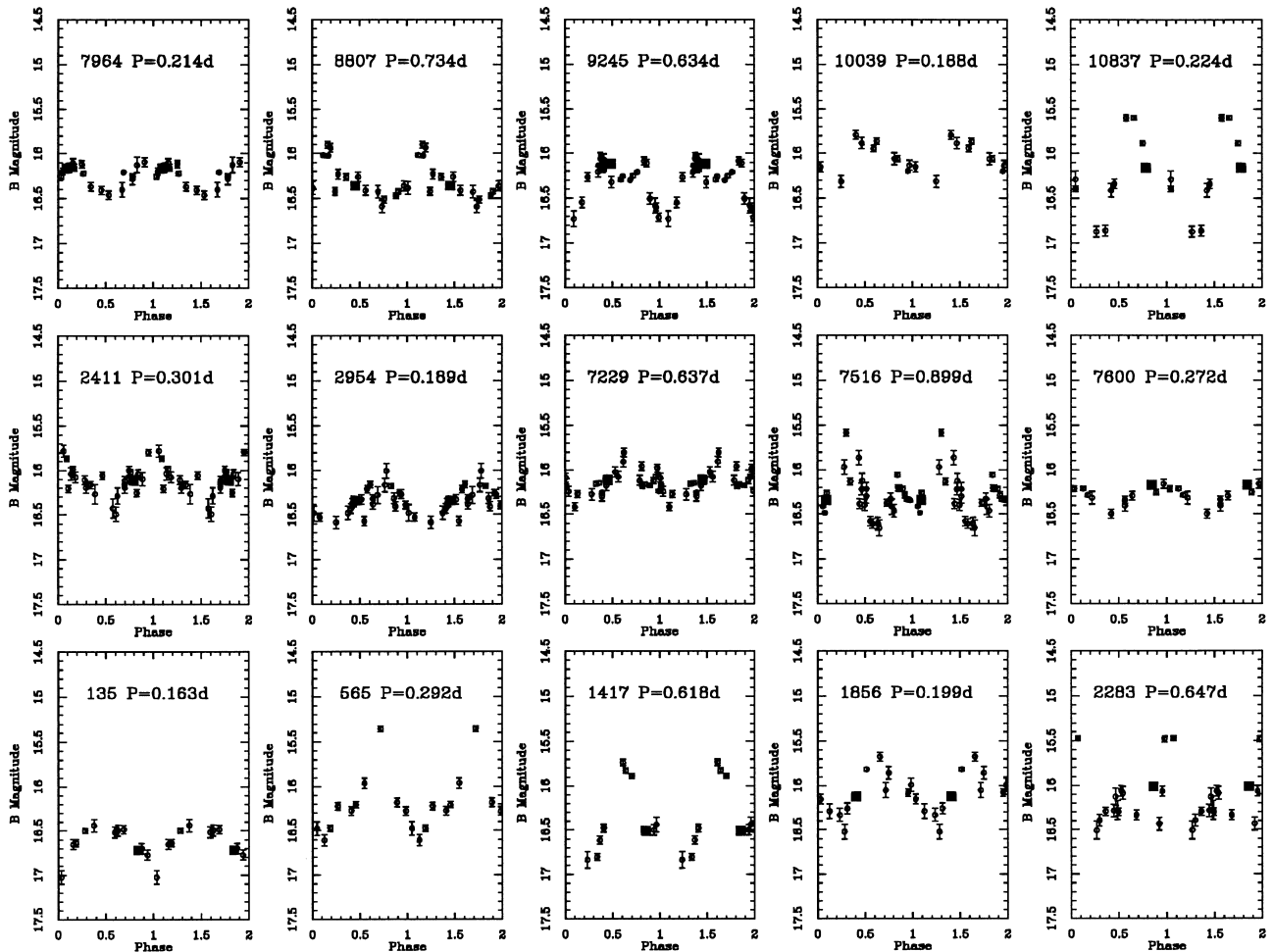
Figure 9. Intrinsic variable star light curves observed in the central region of M15: other variables (primarily new discoveries). The corresponding m_{F439W} point is shown as a filled black square except for the stars where it did not fall in phase. The error bars plotted were computed by ALLSTAR on the basis of crowding and Poissonian noise.

proposed by Diethelm (1990, and references therein), it is most likely an AHB1 type, as indicated by its apparently fast rise time and location in this low-metallicity cluster.

The other four *HST* candidates show marked variability for which we could not determine a regular phase curve. Three of these four ($V17_{HST}$–$V19_{HST}$) are the components of the system that was formerly designated as the single star AC214 (Auriere, Le Fevre & Terzan 1984), and which was first resolved by the *HST*. The probable cause for our failure to see regular variability is their extreme crowding with respect to each other (separations < 0.1 arcsec) and their surroundings, which our technique cannot entirely overcome. Unfortunately, Ferraro & Paresce (1993) do not plot light curves for these three stars, stating that a more accurate analysis will be needed to draw any conclusion concerning the nature of this 'multiple system', so we have no clear picture yet of how these stars behave temporally. Yanny et al. (1994) present comparisons of cusp simulations with their *HST* observations, and suggest that this group may mark the collapsed core (the central cusp) itself. Clearly more observations from space, and from the ground in excellent seeing conditions, are required to identify the multiple variabilities of this system. Our failure to determine a regular phase curve for the fourth *HST* star ($V12_{HST}$) is probably due to its position near the edge of most of the 1992 June images, with a very close companion of similar brightness, which may have skewed its photometry.

We have also detected 15 other variable stars of which 11 appear to be RR Lyraes, as determined by their brightness, colour, period and phase-curve shape. Three others (Nos. 2411, 2954 and 7516), while showing RR Lyrae-like light curves, are located on or near the giant branch of the CMD despite an attempt at colour-lag correction. Another star on the RGB, No. 135, shows a light curve consistent with a partially eclipsing variable. While a few of these 15 may have arisen due to phase-folding on photometric time-series 'noise', most of them are very certain variables; clearly we will need to obtain longer baseline data to confirm the nature and refine the period estimates of these stars. A review of the literature showed that all but one or two of these 15 are newly discovered candidates; while the available astrometry is rather poor, our No. 1417 has almost certainly been detected before as V85, and our No. 565 is probably V83, although the astrometric coincidence is more tentative in this case. V82 lies near the western corner of the PC1 image but was rarely imaged by us. The only previously confirmed intrinsic variable within a radius of 20 arcsec, the long-period W Vir variable V86, varies visibly on our images from 1994 July; however, as it was an ideal sharpening reference star, its photometry was somewhat distorted for the reason given in Section 6.1. In any case, our baseline of three nights would be inadequate to determine the parameters of its cycle. The blue stragglers did not show significant variability at the level of our photometric accuracy.

In this work we have not discussed AC211, the well-known low-mass X-ray binary variable which lies ~2 arcsec from the cluster centre. We shall present our results on this object in a subsequent paper on the binary search.

TRIFFID has now been upgraded to two dedicated variants, TRIFFID-2P and TRIFFID-2R. Both feature a more sensitive MAMA from NASA-GSFC (Danks et al. 1992, 1996); a compact optical design; a faster data collection system capable of storing up to $500\,000$ event s^{-1} sustained; and *simultaneous* multicolour imaging of the same field with the same detector. The improved sensitivity will be highly beneficial, as this was the factor that most limited the photometry of our 1994 July data. Using TRIFFID-2R on 1-m-class telescopes, we have begun to study several globular clusters over much longer periods. This study will produce the most comprehensive survey to date of variable stars in their central regions. The wider, squarer field of view (compared with this study) and simultaneous *B* and *V* photometry will overcome the coverage and colour/phase-lag problems described above, making determination of the variable types a much simpler matter. With the application of the technique that we have shown here, and which we plan to develop further, we expect our future photometry to shed new light on the core populations of these clusters, and thus to complement the detailed but essentially static information that the *HST* gives us.

ACKNOWLEDGMENTS

REFERENCES

Auriere M., Cordoni J.-P., 1981, A&AS, 46, 347
Auriere M., Le Fevre O., Terzan A., 1984, A&A, 138, 415
Carter M. K., Cutler R., Patchett B. E., Read P. D., Waltham N., van Breda I. G., 1990, SPIE, 1235, 644
Cullum M., Wampler E. J., 1990, ESO Messenger, 61, 58
Danks A. C., Joseph C., Bybee R., Argebright V., Abraham J., Kimble R., Woodgate B., 1992, in Pilbratt G., ed., Proc. ESA Symp. ESA-SP 356, Photon Detectors for Space Instrumentation. ESA/ESTEC, Noordwijk, p. 269
Danks A. C. et al., 1996, in Benvenuti P., Macchetto F. D., Schreier E. J., eds, Proc. STScI Symp., Science with the Hubble Space Telescope II. The Space Telescope Science Institute, Baltimore p. 579
Diethelm R., 1990, A&A, 239, 186
Ferraro F. R., Paresce F., 1993, AJ, 106, 154
Fried D. L., 1966, J. Opt. Soc. Am., 56, 1372
Fusi Pecci F., Rosino L., Voli M., 1980, A&A, 85, 269
Guhathakurta P., Yanny B., Schneider D. P., Bahcall J. N., 1996, AJ, 111, 267
Krist J., Hook R., 1996, TINY TIM User's Manual, Version 4.2. The Space Telescope Science Institute, Baltimore, MD
Lucy L. B., 1974, AJ, 79, 745
Lucy L. B., 1992, AJ, 104, 1260
Morris P. W., 1995, UCG Internal Software Report 95S
Phillips A. C., Davis L. E., 1995, in Shaw R. A., Payne H. E., Hayes J. J. E., eds, ASP Conf. Ser. Vol. 77, Astronomical Data Analysis Software and Systems IV. Astron. Soc. Pac., San Francisco, p. 297
Read P. D., Carter M. K., Kent B. J., Swinyard B. M., Patchett B. E., Redfern R. M., Shearer A., Van Breda I. G., 1995, SPIE, 2551, 224R
Redfern R. M., 1991, Vistas Astron., 34, 201
Redfern R. M., Devaney M. N., O'Kane P., Ballestros Ramirez E., Gomez Renasco R., Rosa F., 1989, MNRAS, 238, 791
Redfern R. M., Shearer A., O'Kane P., O'Byrne C., Wouts R., 1992, in Beckers J. M., ed., Proc. Conf., High-resolution imaging by interferometry 2:1991. Ground-based interferometry at visible and infrared wavelengths. European Southern Observatory, Garching, p. 543
Redfern R. M., Shearer A., Wouts R., O'Kane P., O'Byrne C., Jordan B. D., 1993, in Butler C. J., Elliot I., eds, Proc. IAU Colloq. 136, Stellar Photometry – Current techniques and future developments. Cambridge Univ. Press, Cambridge, p. 205
Sawyer-Hogg H., 1973, Publ. David Dunlap Obs., 3, 6, 1
Shearer A., Butler R., Redfern R. M., Cullum M., Danks A. C., 1996, ApJ, 473, L115
Silbermann N. A., Smith H. A., 1995, AJ, 109, 1119
Sosin C., King I. R., 1997, AJ, 113, 1328
Statler T. S., Ostriker J. P., Cohn H. N., 1987, ApJ, 316, 626
Stetson P. B., 1994, PASP, 106, 250
Timothy J. G., Bybee R. L., 1985, SPIE, 687, 1090
Wu N., 1994, in Hanisch R. J., White R. L., eds, Proc. STScI Workshop, The Restoration of *HST* Images and Spectra II. The Space Telescope Science Institute, Baltimore, p. 58
Yanny B., Guhathakurta P., Bahcall J. N., Schneider D. P., 1994, AJ, 107, 1745
Zinn R., 1985, ApJ, 293, 424

This paper has been typeset from a T$_E$X/L^{A}T$_E$X file prepared by the author.